PNAS RESEARCH ARTICLE | MEDICAL SCIENCES OPEN ACCESS

PIK3CA gain-of-function mutation in Schwann cells leads to severe neuropathy and aerobic glycolysis through a non-cell autonomous effect

Quitterie Venot[a,b,c,1], Marina Firpion[a,b,c,1], Sophia Ladraa[a,b,c,1], Charles Bayard[a,b,c], Sato Magassa[a,b], Roberta Di Guardo[d], Antoine Fraissenon[a,b,e,f,g], Clément Hoguin[a,b,c], Sanela Protic[a,b,c], Gabriel Morin[a,b,c], Franck Mayeux[a,b,c], Genevieve Gourdon[h], Sylvie Fraitag[i], Estelle Balducci[a,b,j], Sophie Kaltenbach[a,b,j], Patrick Villarese[a,b,j], Vahid Asnafi[a,b,j], Thomas Viel[k], Gwennhael Autret[k], Bertrand Tavitian[a,k], Nicolas Goudin[l], Laurent Guibaud[b,g], Alessandra Bolino[d,m,1], and Guillaume Canaud[a,b,c,1,2]

Affiliations are included on p. 10.

Edited by Peter Vogt, Scripps Research Institute Department of Molecular Medicine, La Jolla, CA; received November 29, 2024; accepted May 13, 2025

PIK3CA-related disorders are rare genetic disorders due to somatic gain-of-function mutations in _PIK3CA_ during embryonic development, a pathway involved in cell growth, proliferation, and metabolism. Accumulating evidence from patients with _PIK3CA_-related disorders indicates that peripheral nerves are frequently affected, leading to severe neurological symptoms. However, the exact underlying mechanism of these disorders remains unclear. To address this, we developed a mouse model with a _PIK3CA_ gain-of-function mutation specifically in Schwann cells, which successfully mirrored the clinical features observed in patients. In this model, we observed that _PIK3CA_-mutated cells communicate with neighboring healthy cells, such as adipocytes and hair follicles, through a unique crosstalk mechanism that triggers their growth, proliferation, and anagen phase expansion. Additionally, we demonstrated that _PIK3CA_ mutation in peripheral nerves leads to a metabolic shift through glycolytic activation. We investigated the effects of alpelisib, an approved pharmacological inhibitor of PIK3CA, in the model. Early administration of alpelisib significantly improved the signs and symptoms in the mice. However, when treatment was delayed, its efficacy was diminished due to the drug's inability to penetrate the myelin sheath effectively. In summary, our study offers a valuable mouse model for studying _PIK3CA_-related neuropathy, uncovers a unique communication between healthy and affected tissues, and highlights the potential benefits of early pharmacological intervention using alpelisib.

somatic mutation | nerve anomalies | PIK3CA

Significance

Phosphatidylinositol-4,5-bisphosphate 3-kinase (PIK3CA)-related disorders are rare genetic conditions caused by somatic gain-of-function mutations in the PIK3CA gene, affecting cell growth, proliferation, and metabolism. These mutations often impair peripheral nerves, leading to severe neurological symptoms. To investigate this, we developed a mouse model with PIK3CA mutations in Schwann cells, replicating clinical features seen in patients. The study revealed a unique communication between mutated cells and neighboring healthy tissues, promoting growth and metabolic shifts via glycolysis activation. Early treatment with alpelisib, a PIK3CA inhibitor, significantly improved symptoms, but delayed treatment was less effective due to poor myelin penetration. These findings provide insights into disease mechanisms and underscore the importance of timely intervention.

PI3Kα is a ubiquitously expressed lipid kinase that controls signaling pathways participating in cell proliferation, motility, survival, and metabolism (1). At the cellular level, PI3Kα is mainly recruited through tyrosine kinase receptors. *PIK3CA* encodes the 110-kDa catalytic alpha subunit of PI3K (p110α), which converts, at the plasma membrane, phosphatidylinositol 4,5-bisphosphate (PtdIns (4, 5)P_2) to phosphatidylinositol 3,4,5-triphosphate (PtdIns (3, 4, 5) P_3; or PIP3) and subsequently recruits PDK1, which in turn phosphorylates protein kinase B (AKT) on the Thr^{308} residue to initiate downstream cellular effects. PI3Kα also regulates many other pathways, including the Rho/Rac1 signaling cascade (2).

PIK3CA-related disorders are rare genetic conditions due to somatic gain-of-function mutations in the *PIK3CA* gene (3, 4). These mutations occur during embryonic development leading to variable clinical presentation at birth including asymmetrical overgrowth and vascular malformations (called *PIK3CA*-Related Overgrowth Spectrum, PROS) (3). Accumulating pieces of evidence in patients with PROS show that peripheral nerves are frequently involved (3, 5–9). Indeed, patients often experience neurological symptoms including pain, carpal tunnel when the median nerves are affected, difficulty in motricity, and numbness (5–7, 9–13). Certainly, the neurological spectrum of *PIK3CA*-related neuropathy is even broader but not yet fully described. Histologically, the affected nerves exhibit enlargement with a pseudo-onion bulb aspect (7, 12). Typically, these nerves are surrounded and separated by excessive growth of adipose tissue, commonly referred to as lipomatosis of the nerve (14). Currently, it remains unclear whether the somatic mutation primarily affects the nerves themselves or specifically targets the surrounding tissues, including the adipose tissue.

Schwann cells in the peripheral nervous system generate myelin through spiral wrapping of their plasma membrane around axons (15). Peripheral nervous system myelination strictly depends on the fine-tuning of the AKT/mechanistic target of rapamycin (mTOR) pathway downstream of NRG1 (Neuregulin) type III and ErbB2/ErbB3 receptor signaling. Indeed,

This article is a PNAS Direct Submission.

[1]Q.V., M.F., S.L., A.B., and G.C. contributed equally to this work.

[2]To whom correspondence may be addressed. Email: guillaume.canaud@inserm.fr.

This article contains supporting information online at https://www.pnas.org/lookup/suppl/doi:10.1073/pnas.2424867122/-/DCSupplemental.

Published June 24, 2025.

constitutive AKT activation or conditional ablation of Phosphatase and Tensin homolog (PTEN) in Schwann cells in vivo results in focal hypermyelination and aberrant myelin (16, 17). Interestingly, specific loss of PTEN in Schwann cells was associated with inguinal white adipose tissue enlargement (18). Moreover, mTORC1 overactivation has different impacts on myelination depending on the extent and on the timing of the overactivation. Indeed, high mTORC1 activity in the transition from the promyelinating to the myelinating stage hampers Schwann cell proliferation and delays the onset of myelination. On the contrary, high to moderate mTORC1 activity later in nerve development results in focal hypermyelination and in aberrant myelin (19–21). Finally, loss of function of mTORC1 alone or in combination with mTORC2 results in hypomyelination, thus further supporting a key role of mTOR in myelination (22, 23).

All these findings suggest that, upstream of the AKT–mTOR axis, *PIK3CA* gain-of-function mutations in Schwann cells during embryonic development may have a significant impact in myelination. To support this hypothesis, we investigated the consequence of *PIK3CA* gain-of-function mutation in Schwann cells in a preclinical model and then in patients.

Methods

Animals. For this research, we crossed mice with specific genetic characteristics obtained from Jackson Laboratories. We bred homozygous *R26StopFLP110** (Stock# 012343) mice with heterozygous *MPZ-Cre* (Stock# 017927) mice. The resulting offspring were classified as *PIK3CA*$^{MPZ\text{-}Cre+}$ (*R26StopFLP110**+/- x MPZ-Cre+) and *PIK3CA*$^{MPZ\text{-}Cre-}$ (*R26StopFLP110**+/- x *MPZ-Cre*−) mice. The *R26StopFLP110** mice produce a constitutively active p110* protein, which is a chimera consisting of the iSH2 domain of p85 fused to the NH2-terminus of p110 through a flexible glycine linker. In order to create mice with tissue-specific expression of p110*, a loxP-flanked neoR-stop cassette was inserted into a modified version of *pROSA26-1*. This cassette was followed by cDNA encoding *p110**, an frt-flanked IRES-EGFP cassette, and a bovine polyadenylation sequence (*R26StopFLP110**). To track the activity of Cre recombinase, we further crossed *PIK3CA*$^{MPZ\text{-}Cre+}$ and *PIK3CA*$^{MPZ\text{-}Cre-}$ mice with Gt(ROSA)26Sortm4(ACTB-tdTomato,-EGFP)Luo/J mice. These mice express a tdTomato fluorescent protein localized to the cell membrane in all tissues, which is replaced by green fluorescent protein (GFP) upon Cre recombinase activity. Animals were fed ad libitum and housed at a constant ambient temperature in a 12-h light cycle. Animal procedures were approved by the '*Ministère de l'Enseignement Supérieur, de la Recherche et de l'Innovation* (APAFIS N°20439-2018121913526398 and APAFIS N°30133-2020111914293579). All appropriate procedures were followed to ensure animal welfare.

The mice received daily treatment of alpelisib (MedChem Express, Germany; HY-15244) at a dosage of 50 mg kg^{-1} in 0.5% carboxymethylcellulose (Sigma Aldrich). The administration was performed through oral gavage from P21 or P60, or through intraperitoneal injection from P10 to P21.

Morphological Analysis. Mouse tissues were fixed in 4% paraformaldehyde and paraffin embedded. Tissue sections (4 μm thick) were stained with hematoxylin and eosin (H&E).

Semithin Section and Electron Microscopy. Semithin section and ultrastructural analyses of sciatic nerves were performed as follows: Tissues were removed and fixed with 2% glutaraldehyde (vol/vol) in 0.12 M phosphate buffer, postfixed with 1% osmium tetroxide (vol/vol), and embedded in Epon (Epoxy embedding medium SIGMA). Semithin sections (0.5 to 1 μm thick) were stained with toluidine blue and examined by light microscopy (Olympus BX51TF). To perform morphometric analysis, digitalized images cross sections were obtained from corresponding levels of sciatic nerves with 4×, 10×, 20×, or 100× objectives and a Leica DFC7000T digital camera (Milan, Italy).

Sciatic nerves were fixed in 2.5% glutaraldehyde solutions. The prepared samples were examined in a JEOL 1011 transmission electron microscope (JEOL, Japan) with an ORIUS 1000 CCD camera (GATAN, France), operated with Digital Micrograph software (GATAN, France) for acquisition.

Blood and Plasma Analysis. At the conclusion of each experiment, the mice were subjected to blood sample collection using ethylenediaminetetraacetic acid (EDTA)-coated tubes. To determine the blood count, fresh blood samples were analyzed using a hematology analyzer (ProCyte Dx; IDEXX Laboratories) and subsequently centrifuged at 500× g for 15 min. The plasma obtained from the centrifugation was utilized to measure the circulating levels of insulin (U-PLEX Mouse Insulin assay, Meso Scale Discovery, reference no. K1526HK) and IGF-1 (Novus Biologicals, ref#MG100) through enzymatic methods employing commercially available kits.

Open Field. The open-field test was conducted utilizing the Open Field Superflex box, equipped with Fusion software (version 5.3) from Omnitech Electronics (Columbus, OH). The measurements were carried out within a designated mouse room, ensuring protection from external noise and vibrations. To minimize stress, the mice were handled gently. Each mouse was positioned in the center of the cage, and their movements were observed and recorded for a duration of 15 min. Following each test, the cage was thoroughly cleaned using 70% ethanol.

Grip Test. Grip strength performance of the mice was evaluated using a grip strength dynamometer obtained from Bioseb (Chaville, France). To assess hindlimb muscle strength, the mice were positioned on a grid surface. Gentle traction was applied to the mice's tails in the opposite direction, and the maximum strength exerted by each mouse before releasing their grip was measured five times. A recovery period of 30 s was provided between each measurement. The average value from the five measurements was calculated as the indicator of hindlimb grip strength.

Immunohistochemistry and Immunofluorescence. Tissue sections (4 μm thick) embedded in paraffin were subjected to antigen retrieval protocols using high temperature (120 °C) and high pressure in a pressure cooker, utilizing citrate buffer. Subsequently, the sections were incubated with primary antibodies as indicated in *SI Appendix*, Table S1. For the immunofluorescence procedure, the sections were treated with suitable Alexa Fluor-conjugated secondary antibodies (Thermo Fisher Scientific), followed by analysis using an LSM 700 confocal microscope (Zeiss) or Eclipse Ni-E (Nikon). Immunohistochemistry detection was performed using appropriate horseradish peroxidase-linked secondary antibodies and analyzed using E800 (Nikon).

BaseScope Assay. The BaseScope assays were conducted following the guidelines provided by the supplier (Advanced Cell Diagnostics, Newark, CA). The sections were first baked at 60 °C for 1 h and then subjected to deparaffinization in xylene (2 × 5 min) and ethanol (2 × 2 min), followed by drying through baking at 60 °C for 30 min. Pretreat 1 (hydrogen peroxide) was applied at room temperature for 10 min, followed by Pretreat 2 (target retrieval) at 100 °C for 15 min and Pretreat 3 (protease IV) at 40 °C for 30 min. BaseScope probes, such as BA-Hs-PPiB-1zz as a positive control, BA-DapB-1zz as a negative control, or Ba-HS-PIK3CA-H1047R, were then applied at 40 °C for 2 h in a HybEZ oven. Subsequently, the sections were incubated with reagents AMP1 (40 °C, 30 min), AMP2 (40 °C, 30 min), AMP3 (40 °C, 15 min), AMP4 (40 °C, 30 min), AMP5 (40 °C, 30 min), AMP6 (40 °C, 15 min), AMP7 (room temperature, 30 min), and AMP8 (room temperature, 15 min). Finally, the slides were incubated with Fast Red for 10 min at room temperature in the dark, counterstained with Mayer Hemalun, dried for 15 min at 60 °C, and mounted in EcoMount permanent mounting medium (Biocare Medical, Pacheco, CA). The slides were analyzed using E800 (Nikon).

Sciatic Nerve Explant Culture. Sciatic nerve was removed carefully from the mice and placed into culture dishes and maintained free-floating in Dulbecco's Modified Eagle Medium containing: 2 mM L-glutamine, 100 U/mL penicillin, 100 mg/mL streptomycin, in an atmosphere of 95% air and 5% CO_2 at 37 °C. Explants were exposed to Alpelisib (MedChem Express, Germany; HY-15244) or DMSO for 8 h. Tissues were then harvested, washed in phosphate-buffered saline, and powdered for western blot experiments.

Western Blot. The tissues were crushed and subsequently lysed using radio immunoprecipitation assay lysis buffer containing phosphatase and protease inhibitors. The protein concentrations were determined using the bicinchoninic acid method (Pierce). Following that, the protein extracts were separated by SDS-PAGE and transferred onto the suitable membrane. The membrane was then incubated with the primary antibody (*SI Appendix*, Table S1), followed by the appropriate peroxidase-conjugated secondary antibody (at a dilution of 1:10,000). Chemiluminescence signals were detected using Chemidoc MP, and the bands were quantified using Image Lab Software from Bio-Rad Laboratories.

Messenger ribonucleic acid (mRNA) Analysis. qPCR with reverse transcriptase was employed to quantify mRNAs in mouse tissues using CFX Connect from Bio-Rad. The primers utilized for this analysis can be found in *SI Appendix*, Table S2.

Imaging Flow Cytometry (ImageStream). Skin samples were subjected to digestion using a digestion buffer. Subsequently, the cells were transferred to microtubes and analyzed using an Imagestream ISX mkII system (Amnis). This system integrates flow cytometry with comprehensive cell imaging and functional studies. Acquisitions were performed at a magnification of 40× for all samples. Data acquisition was conducted using INSPIRE software (Amnis), and the obtained data were analyzed using IDEAS software (version 6.2, Amnis).

Targeted Liquid Chromatography–Mass Spectrometry (LC–MS) Metabolites Analyses. Blood samples were collected using EDTA tubes for plasma analysis and EDTA-free tubes for serum analysis. After centrifugation of the blood at 500 g for 10 min, plasma and serum were obtained. Cell, plasma, and serum samples were immediately snap-frozen in liquid nitrogen. For the extraction of metabolites in preparation for LC–MS analyses, the extraction solution composed of 50% methanol (MeOH), 30% acetonitrile, and 20% water was used. The volume of the extraction solution added was adjusted according to the cell number (1 mL per 1 million cells) or the volume of plasma and serum (200 μL per 10 μL of plasma or serum). After the addition of the extraction solution, the samples were vortexed for 5 min at 4 °C and then centrifuged at 16,000 g for 15 min at 4 °C. The supernatants were collected and stored at −80 °C until further analyses.

The LC–MS analyses were carried out using a Q Exactive Plus Orbitrap mass spectrometer equipped with an Ion Max source and a HESI II probe, coupled to the Dionex UltiMate 3000 UPLC System from Thermo Fisher Scientific. External mass calibration was performed using the standard calibration mixture every 7 d as per the manufacturer's recommendation. Five microliters of each sample were injected onto a ZIC-pHILIC column (150 mm × 2.1 mm inner diameter, 5 μm) with a guard column (20 mm × 2.1 mm inner diameter, 5 μm; Millipore) for LC separation. The chromatographic gradient was run at a flow rate of 0.200 μL/min, with buffer A as 20 mM ammonium carbonate and 0.1% ammonium hydroxide (pH 9.2) and buffer B as acetonitrile. The gradient conditions were as follows: from 0 to 20 min, a linear gradient from 80 to 20% B; from 20 to 20.5 min, a linear gradient from 20 to 80% B; and from 20.5 to 28 min, holding at 80% B.

The mass spectrometer operated in full scan polarity switching mode, with the spray voltage set to 2.5 kV and the heated capillary held at 320 °C. The sheath gas flow was set to 20 U, the auxiliary gas flow was set to 5 U, and the sweep gas flow was set to 0 U. The metabolites were detected across a mass range of 75 to 1,000 mass-to-charge ratio (m/z) at a resolution of 35,000 (at 200 m/z) with the AGC target set to 106 and a maximum injection time of 250 ms. Lock masses were used to ensure mass accuracy below five parts per million. Data acquisition was performed using Thermo Xcalibur 4.0.27.13 software, and the peak areas of metabolites were determined using Thermo TraceFinder 3.3 SP1 software. The metabolites were identified based on their exact mass of each singly charged ion and known retention time in the high-performance LC (HPLC) column.

2′-Deoxy-2′-[18F]Fluoro-D-Glucose (FDG) Positron Emission Tomography Computed Tomography (PET-CT) Imaging. Ten mice (*PIK3CA*$^{MPZ\text{-}Cre-}$: two females, three males; *PIK3CA*$^{MPZ\text{-}Cre+}$: three females, two males) underwent overnight fasting with unrestricted access to water. The mice were anesthetized with 1.9 ± 0.4% isoflurane in dioxygen, weighed, and their blood glucose levels were measured by drawing blood from the caudal ventral artery using an Accu-Chek® Aviva Nano A glucose meter (Accu-Chek, France). A 29G needle catheter (Fischer Scientific, France) connected to a 5 cm polyethylene tubing (Tygon Microbore Tubing, 0.010″ × 0.030″ OD; Fisher Scientific, France) was inserted into the caudal vein for radiotracer injection. A total of 9.4 ± 1.3 MBq of FDG (Advanced Applied Applications, France) in 0.2 mL saline was injected through the catheter. The mice were kept anesthetized on a warming plate for 45 min and then positioned on the dedicated PET-CT bed. Respiration and body temperature were monitored throughout the procedure. The body temperature was maintained at 34 ± 2 °C, and anesthesia levels were adjusted based on the breathing rate during the entire PET-CT examination.

CT scans were acquired using a PET-CT scanner (nanoScan PET-CT; Mediso Medical Imaging Systems, Hungary) with the following acquisition parameters: semicircular mode, 50 kV voltage, 360 full scan projections, 170 ms per projection, and binning 1:4. The CT projections were reconstructed using filtered retroprojection (filter: Cosine; Cutoff: 100%) with Nucline 3.00.010.0000 software (Mediso Medical Imaging Systems, Hungary). At 55 min posttracer injection, PET data were collected for 10 min in list mode and binned using a 5 ns time window, 400 to 600 keV energy window, and 1:5 coincidence mode. The data were reconstructed using the TeraTomo reconstruction engine, a three dimensional (3D)-OSEM-based customized algorithm, incorporating scatter and attenuation correction.

Volumes-of-interest (VOIs) were delineated on the organs or anatomical structures of interest on PET/CT fusion slices using the PMOD software package (PMOD Technologies Ltd, Zürich, Switzerland). Spherical VOIs were drawn based on CT and PET information. The VOIs, including the sciatic nerves, were automatically segmented at 75% and 33% of the maximum value. FDG accumulation was quantified as the Standard Uptake Value, which represents the ratio of the radioactivity concentration in the VOI to the whole-body concentration of the injected radioactivity.

Ex Vivo FDG Uptake Assessment by Gamma Counting and Autoradiography. Twelve mice (*PIK3CA*$^{MPZ\text{-}Cre-}$: two females, five males; *PIK3CA*$^{MPZ\text{-}Cre+}$: two females, three males) underwent overnight fasting with unrestricted access to water. The mice were anesthetized using 2.0% isoflurane in dioxygen, weighed, and their blood glucose levels were measured by drawing blood from the caudal ventral artery using an Accu-Chek® Aviva Nano A glucose meter (Accu-Chek, France). A 29G needle catheter (Fischer Scientific, France) connected to a 5 cm polyethylene tubing (Tygon Microbore Tubing, 0.010″ × 0.030″ OD; Fisher Scientific, France) was inserted into the caudal vein for radiotracer injection. A total of 7.9 ± 1.6 MBq of FDG (Advanced Applied Applications, France) in 0.2 mL saline was injected via the catheter, alternating between CRE+ and CRE− mice. The mice were kept anesthetized on a warming plate for 55 min and then killed by cervical dislocation. The right and left sciatic nerves were dissected.

The right sciatic nerves were placed in counting vials, and their weight and accumulated radioactivity were measured using a gamma counter (Hidex AMG Automatic Gamma Counter, Hidex AMG) with the following parameters: 30 s counting time, energy window: 480 to 558 keV, counting efficiency: 0.213.

The left sciatic nerves were exposed to dedicated phosphor imaging plates (GE Healthcare) for 2.5 d. The phosphor imaging plates were scanned with a pixel size of 50 μm using the AmershamTM Typhoon IP (Cytiva).

MRI Evaluation. The mice were subjected to MRI for the entire body using T2 weighted sequences with fat saturation. Additionally, focused MRI of the brain was conducted using T1 and T2 weighted sequences. The assessment of peripheral myelin volume on the MRI scans was performed using IntelliSpace Portal software (Philips Healthcare) and 3D Slicer, utilizing manual segmentation tools. The volume was calculated by summing images based on 2D contours and the slice thickness. Furthermore, the thickness of the skin was measured at the vertex of each animal.

LC–MS Analysis of Alpelisib. Each tissue type was homogenized in 100% cold methanol (MeOH) at a tissue-to-solvent ratio of 1 mg tissue to 5 μL MeOH. After sonication for 20 s, the tissue extract underwent centrifugation at 13,000 g for 30 min, followed by injection onto a Phenomenex Kinetex XB-C18 HPLC column (100 mm by 2.1 mm) at 45 °C. Reverse-phase HPLC analysis of Alpelisib was performed using a Shimadzu LCMS system 8040 with LabSolutions software. For separation, 20 micrograms of tissue extracts were injected onto the column. The mobile phase consisted of two eluants: Solvent A, which was 0.1% formic acid in deionized water (ddH_2O), and solvent B, which was acetonitrile with 0.1% formic acid. Compounds were separated using a discontinuous gradient at a flow rate of 0.6 mL/min. The initial concentration of 20% in solvent B increased to 70% over 6 min, followed by a decrease to 20% over the next minute, and the initial conditions were then maintained for 14 min. Alpelisib was monitored using spectrophotometric absorbance (photodiode detector) in the wavelength range of 205 to 600 nm, as well as tandem mass detection. Mass measurement was performed in positive ion mode using multiple reaction monitoring (MRM) with an electrospray ionization source. Three MRM transitions were used for alpelisib: 442.1 > 328.0, 442.1 > 288.0, and 442.1 > 115.1. Quantification was carried out by integrating the peak absorbance area using a calibration curve established with various known concentrations of alpelisib.

Statistics. Data were expressed as the means ± SEM. Survival curves were analyzed with the Mantel–Cox (log-rank) test. Differences between the experimental groups were evaluated using ANOVA, followed by the Tukey–Kramer post hoc

test when the results were significant ($P < 0.05$). When only two groups were compared, Mann–Whitney tests were used. The statistical analysis was performed using GraphPad Prism software (version 10.0.0).

Results

A Mouse Model of PIK3CA Gain-of-Function in Schwann Cells. We took advantage of the transgenic mouse strain, *R26StopFLP110**, which, after breeding with *Cre* recombinase mice, express a dominant active *PI3KCA* transgene. *R26StopFLP110** mice were crossed with *Mpz Cre* mice to generate $PIK3CA^{MPZ\text{-}Cre+}$ animals that express a constitutively overactivated form of PIK3CA specifically in Schwann cells starting from E12.5 (24). In order to follow the *Cre* recombination, $PIK3CA^{MPZ\text{-}Cre+}$ mice were then interbred with $Gt(ROSA)26Sor^{tm4(ACTB\text{-}tdTomato,\text{-}EGFP)Luo/J}$ mice. These mice express in all tissues a cell membrane localized tdTomato fluorescent protein, that is replaced by GFP after *Cre* recombination. Littermate mice carrying *Mpz Cre* recombinase without *PIK3CA* transgene were used as controls (referred thereafter as $PIK3CA^{MPZ\text{-}Cre-}$).

$PIK3CA^{MPZ\text{-}Cre+}$ mice were born at a Mendelian ratio and had no particular phenotype at birth. However, around P21 of age, mutant mice started to develop tremor with progressive hair extension (Fig. 1*A*). Around the age of P60, both male and female mice began to lose weight (Fig. 1*B*). Neurological symptoms progressed then rapidly with severe tremor, difficulty in walking, very long hair (*SI Appendix*, Fig. S1*A*), chronic hypoglycemia (Fig. 1*C*), and finally significantly reduced survival rate (median survival 16 wk) (Fig. 1*D*). Functional test performed at the age of P21 revealed that $PIK3CA^{MPZ\text{-}Cre+}$ mice had a significantly reduced walking distance, a longer resting time period, a reduced velocity, and less strength compared to controls (Fig. 1*E*). These anomalies worsened with aging (Fig. 1*F*). Whole-body T2-weighted MRI at the age of P90 showed the presence of diffuse neurolemma hypertrophy with the presence of neurofibroma only in $PIK3CA^{MPZ\text{-}Cre+}$ mice compared to controls (Fig. 1*G*). We then killed 20 $PIK3CA^{MPZ\text{-}Cre+}$ and 20 control mice at the age of P90 when the disease was already severely affecting the mice. Necropsy revealed macroscopic bilateral enlargement of sciatic nerves and brachial plexus nerves with no other anatomical anomalies (Fig. 1*H* and *SI Appendix*, Fig. S1*B*). Complete blood count did not reveal any particular alteration (*SI Appendix*, Fig. S1*C*). Nerve enlargement was confirmed by semithin section analysis of sciatic nerves which showed significantly increased area of transverse sections (Fig. 1*H*). The density of myelinated fibers was significantly reduced in mutant nerves and the majority of myelinated fibers were aberrantly myelinated with myelin degeneration and tomacula (Fig. 1*I* and *SI Appendix*, Fig. S1 *D–F*). Western blot and immunofluorescence studies confirmed AKT/mTOR pathway activation in Schwann cells of $PIK3CA^{MPZ\text{-}Cre+}$ mice compared to $PIK3CA^{MPZ\text{-}Cre-}$ (Fig. 1*J* and *SI Appendix*, Fig. S1*G*). Amnis ImageStream® system confirmed that Schwann cells isolated from $PIK3CA^{MPZ\text{-}Cre+}$ mice were hypertrophic compared to controls (Fig. 1*K* and *SI Appendix*, Fig. S2*A*). In addition, we observed enlargement of the skin thickness with disorganized and excessive adipose tissue surrounding the enlarged nerves (Fig. 1 *L* and *M* and *SI Appendix*, Fig. S2*B*). We also noticed hair follicles hypertrophy (Fig. 1*M*). Skin thickness was increased due to hypoderm enlargement (Fig. 1*N*). These findings were consistent with what was observed in patients (Fig. 1*O* and *SI Appendix*, Fig. S2 *C* and *D*).

To better characterize nerve degeneration in this model, we examined sciatic nerves at different time points of postnatal nerve development. At P7, we observed that the area of mutant sciatic nerves was not significantly increased, but the number of fibers that had myelinated was significantly reduced with many fibers that had completed axonal sorting but still devoid of myelin as compared to control nerves (*SI Appendix*, Fig. S3*A*). These findings suggest that overactivation of PI3K-mediated signaling delays the onset of myelination. This conclusion was further supported by semithin section analysis of sciatic nerves at P18 (*SI Appendix*, Fig. S3*B*). At this time point, the number of fibers that had myelinated was significantly increased in the mutant as compared with P7, but still significantly reduced as compared with controls at P18 (*SI Appendix*, Fig. S3 *A* and *B*). Some myelinated fibers showed reduced myelin thickness, whereas approximately 15.6% displayed aberrant myelin, particularly tomacula and aberrant folding, which was already present at P7 (*SI Appendix*, Fig. S3*A*). The area of mutant sciatic nerves was significantly increased as compared with controls. Interestingly, we observed many fibers carrying enlarged cytoplasmic areas surrounding the nucleus, suggesting increased cytoplasmic volumes and shorter internodal length (*SI Appendix*, Fig. S3*B*). Surprisingly, the majority of fibers with aberrant myelin were already degenerated at P30 (approximately 35%), while reduced myelin thickness was more evident in other myelinated fibers of mutant nerves (*SI Appendix*, Fig. S3 *C* and *D*). The number of myelinated fibers as well as their density was significantly reduced in mutant nerves with evident loss of fibers already at this stage which then exacerbates at P90 (*SI Appendix*, Fig. S3 *C* and *D*).

Overall, these data suggest that constitutive *PIK3CA* activation in Schwann cells starting from E12.5 severely affects myelination, causing the formation of abnormal myelinated fibers. These fibers deteriorate quickly, leading to the loss of fibers and resulting in a severe clinical outcome.

In order to gain a deeper understanding of the increased amount of adipose tissue around the nerves and the enlarged hair follicles, we sought to determine where *Cre* recombinase was activated. Using immunostaining and flow cytometry we confirmed that the GFP, and indeed the *Cre* recombinase, was only expressed in Schwann cells and not leaking either in adipocytes nor hair follicles (Fig. 2 *A* and *B* and *SI Appendix*, Fig. S3*E*). The data imply the existence of a potential communication or interaction between the mutated cells and the neighboring cells. To strengthen the evidence of potential crosstalk and to validate our findings in humans, we utilized BaseScope™ in situ hybridization technology with the *PIK3CA H1047R* probe on biopsies taken from patients with *PIK3CA*-related neuropathies who carried this specific variant. Remarkably, we observed that the mutation was exclusively detectable in Schwann cells and not in adipocytes or hair follicles. (Fig. 2 *C–E*). Importantly, while adipocytes were not carrying PIK3CA mutation, they demonstrated increased AKT phosphorylation compared to control skins (Fig. 2 *F* and *G*). Similar observations were made in mice (*SI Appendix*, Fig. S4*A*). Finally, we compared the intensity of P-AKT in the nerves of mice and in patients. As we previously reported (4), we observed that mutant mice demonstrated a higher degree of AKT activation compared to patients (*SI Appendix*, Fig. S4*B*). Collectively, these findings provide strong evidence for communication between mutated cells and neighboring cells, leading to the activation of the AKT pathway.

Interestingly, an increase in skin thickness and hair follicle numbers in $PIK3CA^{MPZ\text{-}Cre+}$ mice may suggest anomalies in this cycle. Hair follicles go through specific stages of cycle: anagen (growth), catagen (regression), and telogen (quiescent) (25). During the anagen phase, hair growth is accompanied by the expansion of intradermal adipocytes, which doubles the thickness of the skin (25, 26). In $PIK3CA^{MPZ\text{-}Cre+}$ mice, we observed a continuous expansion of the skin thickness with enlarged adipocytes, increased proliferation of hair follicle cells, and a higher density of hair follicles (*SI Appendix*, Fig. S4 *C–E*). To assess hair growth propensity, we partially shaved $PIK3CA^{MPZ\text{-}Cre+}$ mice and age-matched

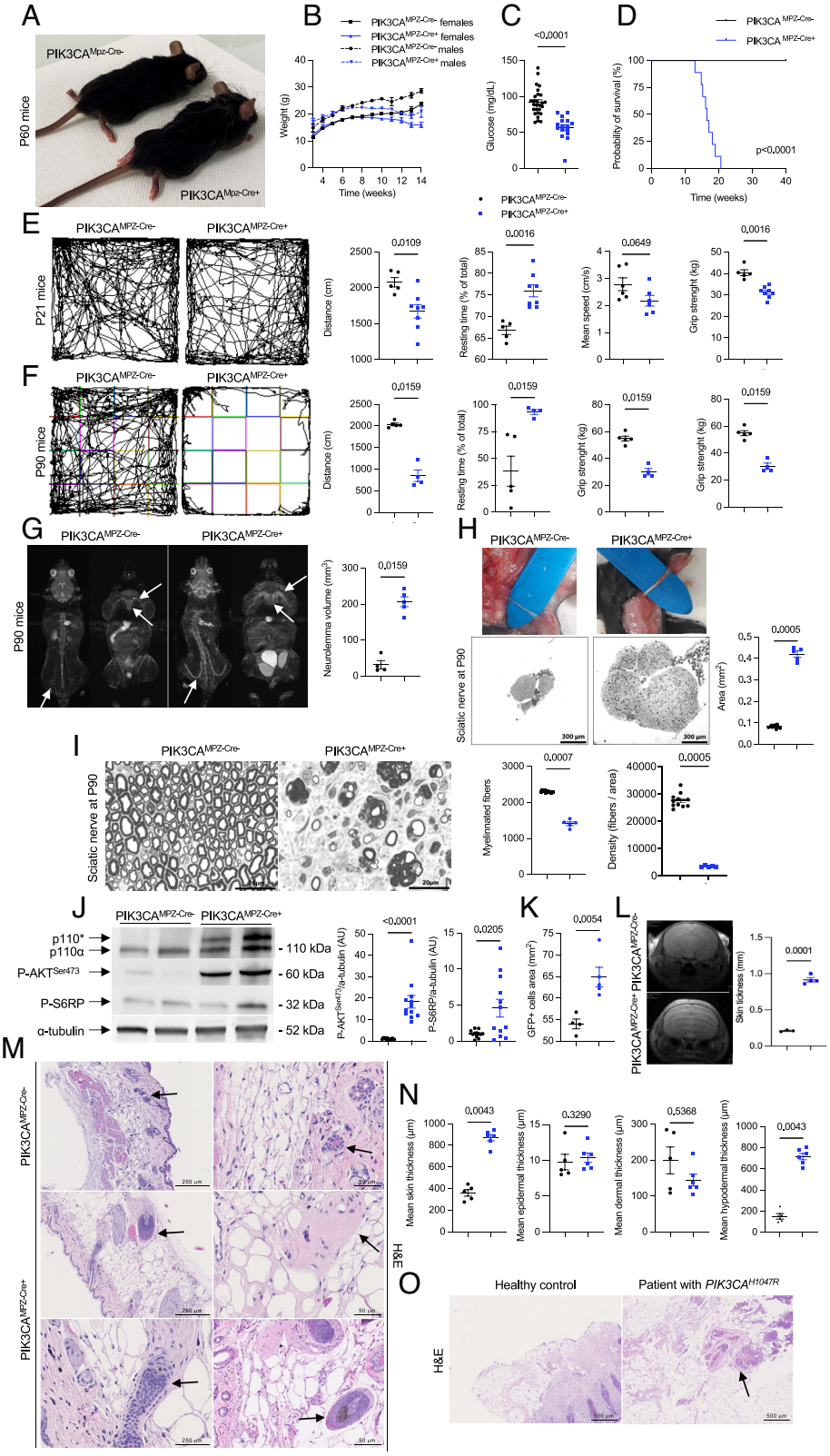

Fig. 1. A mouse model of *PIK3CA*-related peripheral nerve overgrowth. (*A*) Representative photography of *PIK3CA*$^{MPZ\text{-}Cre-}$ and *PIK3CA*$^{MPZ\text{-}Cre+}$ mice at the age of P60. (*B*) Male and female body weights of *PIK3CA*$^{MPZ\text{-}Cre-}$ and *PIK3CA*$^{MPZ\text{-}Cre+}$ mice. (*C*) Twelve-hour fasted glycemia in *PIK3CA*$^{MPZ\text{-}Cre-}$ and *PIK3CA*$^{MPZ\text{-}Cre+}$ mice. (*D*) Kaplan–Meier survival curves of *PIK3CA*$^{MPZ\text{-}Cre-}$ and *PIK3CA*$^{MPZ\text{-}Cre+}$ mice. (*E*) Open field functional test and evaluation of *PIK3CA*$^{MPZ\text{-}Cre-}$ and *PIK3CA*$^{MPZ\text{-}Cre+}$ mice at the age of P21. (*F*) Open field functional test and evaluation of *PIK3CA*$^{MPZ\text{-}Cre-}$ and *PIK3CA*$^{MPZ\text{-}Cre+}$ mice at the age of P90. (*G*) Coronal whole-body T2-weighted MRI of *PIK3CA*$^{MPZ\text{-}Cre-}$ and *PIK3CA*$^{MPZ\text{-}Cre+}$ mice. Neurolemma volume quantification. (*H*) Representative pictures and semithin sections of sciatic nerves of *PIK3CA*$^{MPZ\text{-}Cre-}$ and *PIK3CA*$^{MPZ\text{-}Cre+}$ mice at P90 with nerve section area quantification. (*I*) Semithin sections of sciatic nerves of *PIK3CA*$^{MPZ\text{-}Cre-}$ and *PIK3CA*$^{MPZ\text{-}Cre+}$ mice at P90 with myelinated fibers and density quantification (myelinated fibers on area). (*J*) Western blot and quantification of p110, AKT phosphorylation at Ser^{473} and S6RP in sciatic nerves of *PIK3CA*$^{MPZ\text{-}Cre-}$ and *PIK3CA*$^{MPZ\text{-}Cre+}$ mice. (*K*) Quantification of GFP-positive Schwann cell area of *PIK3CA*$^{MPZ\text{-}Cre-}$ and *PIK3CA*$^{MPZ\text{-}Cre+}$ mice using AmnisImageStream. (*L*) Axial T2-weighted MRI of the head and quantification of the skin thickness of *PIK3CA*$^{MPZ\text{-}Cre-}$ and *PIK3CA*$^{MPZ\text{-}Cre+}$ mice aged of P90. (*M*) Representative H&E staining of skin section of *PIK3CA*$^{MPZ\text{-}Cre-}$ and *PIK3CA*$^{MPZ\text{-}Cre+}$ mice aged of P90. Arrows indicate hair follicles. (*N*) Quantification of the different skin layers of *PIK3CA*$^{MPZ\text{-}Cre-}$ and *PIK3CA*$^{MPZ\text{-}Cre+}$ mice aged of P90. (*O*) Representative H&E staining in skin biopsies from healthy controls and in patients with *PIK3CA*-related nerve anomalies. Arrows indicate hair follicles.

controls. At 9 wk of age, *PIK3CA*$^{MPZ\text{-}Cre+}$ mice showed a faster coverage of the shaved area (*SI Appendix*, Fig. S4*F*). Indeed, these findings suggest a potential crosstalk between mutated Schwann cells and hair follicles that promotes the anagen phase.

Patients with nerve anomalies related to *PIK3CA* mutations may exhibit chronic hypoglycemia. However, the underlying reasons for these anomalies are elusive. We recently reported that the presence of *PIK3CA* gain-of-function mutation specifically in adipocytes was associated with GLUT4 translocation at the cell surface membrane with permanent glucose entry into adipocytes leading to chronic hypoglycemia with low insulin circulating levels due to negative feedback on insulin secretion (27). Considering that the *PIK3CA*$^{MPZ\text{-}Cre+}$ mice exhibited hypoglycemia, we opted to measure insulin levels and observed significantly reduced

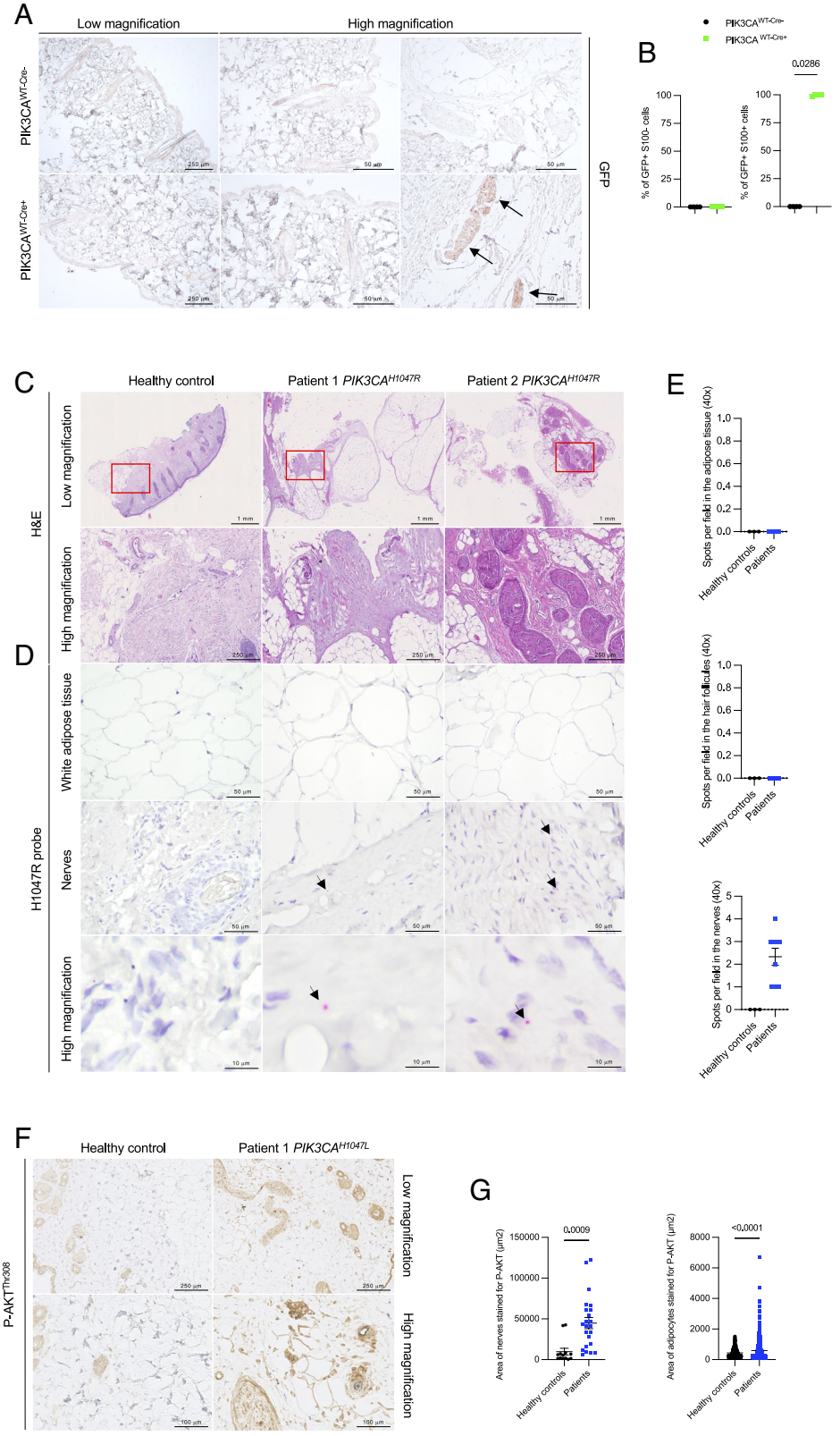

Fig. 2. *PI3KCA* gain-of-function mutations in Schwann cells activate the AKT pathway in surrounding adipocytes and hair follicles. (*A*) Representative immunostaining of GFP in the skin of *PIK3CA*$^{WT\text{-}Cre-}$ and *PIK3CA*$^{WT\text{-}Cre+}$ mice. (*B*) Flow cytometry of GFP and S100 costaining of cells isolated from the skin of *PIK3CA*$^{WT\text{-}Cre-}$ and *PIK3CA*$^{WT\text{-}Cre+}$ mice. (*C*) Representative H&E staining of skin biopsies from healthy controls and patients with *PIK3CA*-related neuropathies. (*D*) In situ hybridization using BaseScope assay of *PIK3CA* H1047R probe in the skin of healthy controls and patients with PIK3CA-related nerve disorders. Arrows show pink dots of hybridization. (*E*) Quantification of the number of spots localized either in the hair follicle, adipose tissue, or nerves. (*F*) Representative immunostaining of P-AKT^{Thr308} in the skin of healthy controls and patients with *PIK3CA*-related neuropathies and (*G*) Quantification.

circulating levels compared to the control group (Fig. 3*A*). Similar to our previous findings in mice harboring a gain-of-function mutation in *PIK3CA* within adipose tissue (27), we observed that in *PIK3CA*$^{MPZ\text{-}Cre+}$ mice reduced levels of insulin correlated with a decrease in the size of the β islets (*SI Appendix*, Fig. S5*A*). Additionally, these mice displayed low circulating levels of IGF1 (*SI Appendix*, Fig. S5*B*), reduced expression of *Igf1* mRNA in the liver (*SI Appendix*, Fig. S5*C*), and a surge in the synthesis of liver IGFBP1 (*SI Appendix*, Fig. S5 *D* and *E*). We ruled out Cre leakage in skeletal muscle or in the liver as a possible explanation for the hypoglycemia (*SI Appendix*, Fig. S5*F*). GLUT1 is the main glucose transporter in peripheral nerves and is expressed in perineurium (28). We stained the tissue section and did not notice any difference of GLUT1 or GLUT 3 expression in the perineurium of

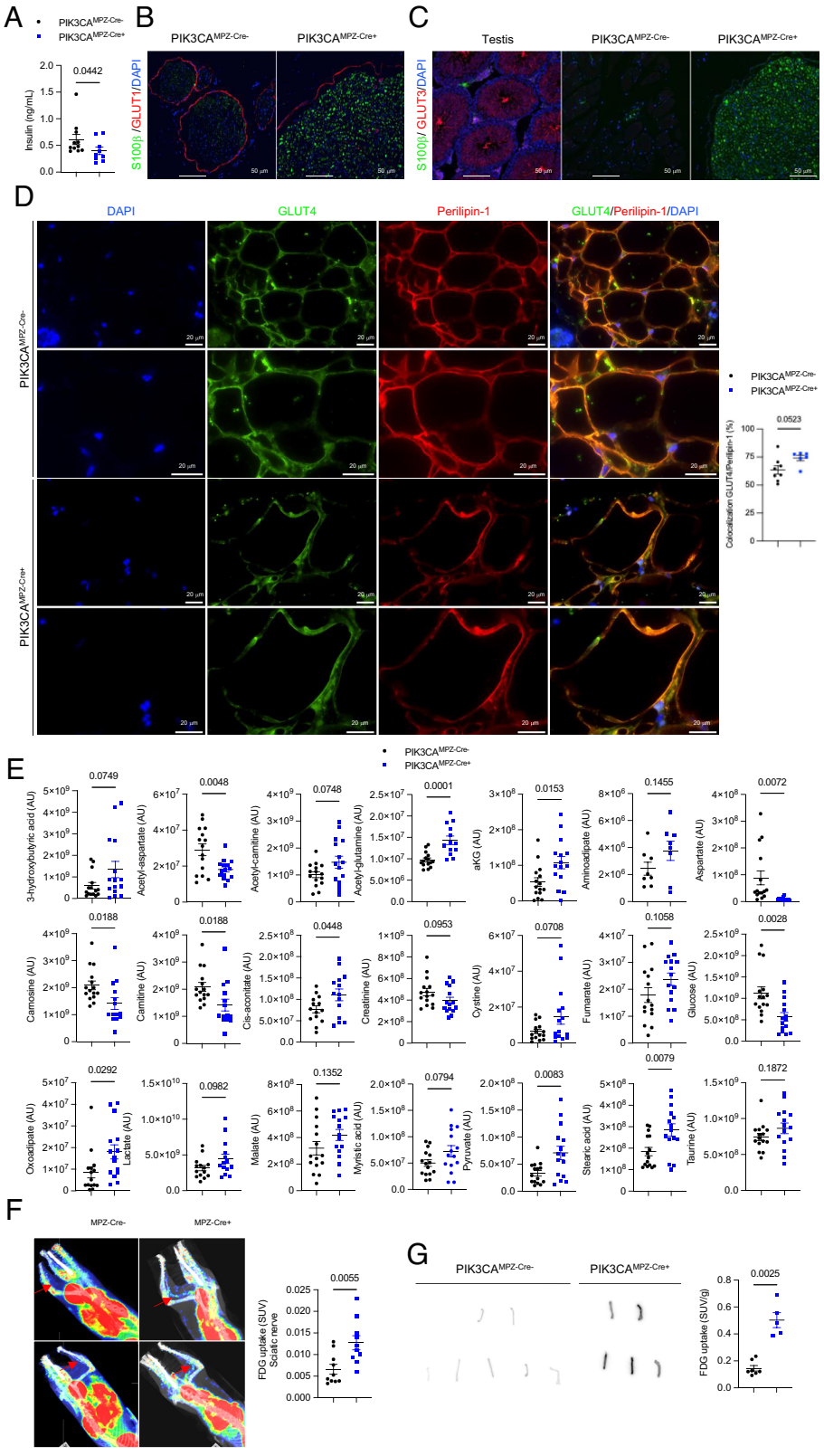

Fig. 3. *PIK3CA*$^{MPZ\text{-}Cre+}$ mice present severe endocrine disruption with features of aerobic glycolysis. (*A*) Insulin circulating levels in *PIK3CA*$^{MPZ\text{-}Cre-}$ and *PIK3CA*$^{MPZ\text{-}Cre+}$ mice. (*B*) Representative immunofluorescence costaining of GLUT1 and S100β in sciatic nerves of *PIK3CA*$^{MPZ\text{-}Cre-}$ and *PIK3CA*$^{MPZ\text{-}Cre+}$ mice. (*C*) Representative immunofluorescence costaining of GLUT3 and S100β in sciatic nerves of *PIK3CA*$^{MPZ\text{-}Cre-}$ and *PIK3CA*$^{MPZ\text{-}Cre+}$ mice. Testis was used as a positive control. (*D*) Representative immunofluorescence costaining of GLUT4 and Perilipin-1 in surrounding areas of the sciatic nerves of *PIK3CA*$^{MPZ\text{-}Cre-}$ and *PIK3CA*$^{MPZ\text{-}Cre+}$ mice and quantification. (*E*) Graphic example of metabolite modification observed in the plasma of *PIK3CA*$^{MPZ\text{-}Cre-}$ and *PIK3CA*$^{MPZ\text{-}Cre+}$ mice. AU: Arbitrary units. (*F*) 18F-fluorodeoxyglucose uptake in sciatic and brachial of *PIK3CA*$^{MPZ\text{-}Cre-}$ and *PIK3CA*$^{MPZ\text{-}Cre+}$ mice. (*G*) Gamma scintigraphy of isolated sciatic nerves of *PIK3CA*$^{MPZ\text{-}Cre-}$ and *PIK3CA*$^{MPZ\text{-}Cre+}$ mice.

PIK3CA$^{MPZ\text{-}Cre+}$ compared to control mice (Fig. 3 *B* and *C*). We then stained the slides for GLUT4 and found that adipocytes surrounding the nerves of the *PIK3CA*$^{MPZ\text{-}Cre+}$ mice had GLUT4 accumulation at the cell membrane compared to controls (Fig. 3*D*). This finding, along with AKT phosphorylation, suggests that the accumulation of GLUT4 and the involvement of adipocytes may contribute to the chronic hypoglycemia observed in mice. Therefore, it is plausible that Schwann cells early in development release paracrine factor(s) that have the ability to activate the AKT pathway in surrounding cells, thereby potentially contributing to the development of chronic hypoglycemia.

We thus conclude that we created a mouse model that faithfully reproduces the phenotype observed in patients with *PIK3CA*-related nerve anomalies.

***PIK3CA*$^{MPZ\text{-}Cre+}$ Mice Demonstrated Metabolic Shift Toward Aerobic Glycolysis.** We previously reported that *PIK3CA* gain-of-function mutation in adipocytes was associated with Warburg-like effect (27). Since we observed similar biological anomalies in *PIK3CA*$^{MPZ\text{-}Cre+}$ mice with severe hypoglycemia and low circulating insulin levels, we examined the plasma of *PIK3CA*$^{MPZ\text{-}Cre+}$ and control mice. Metabolomic analysis of 12 wk old aged mice demonstrated features of aerobic glycolysis with increased lactate and pyruvate production, ketone formation (3 beta hydroxybutyric acid), with increase in several tricarboxylic acid cycle intermediates such as aKG, cis-aconitate, fumarate, or malate, increase in fatty acid products such as myristic acid and carnitine consumption (Fig. 3*E*). Taken together, these data suggest that *PIK3CA*$^{MPZ\text{-}Cre+}$ mice exhibit Warburg-like effect with the biosynthesis of macromolecules.

To validate the metabolic switch, we conducted FDG uptake assays. Consistently, we observed a significant increase in FDG uptake in the peripheral nerves of *PIK3CA*$^{MPZ\text{-}Cre+}$ mice compared to the control group (Fig. 3*F*). In order to demonstrate that the increased FDG uptake was a result of potential aerobic glycolysis and not solely influenced by the surrounding adipose tissue, we isolated sciatic nerves from both mutant and control mice aged 12 wk. Gamma scintigraphy confirmed that FDG uptake was only observed in the mutant nerves, distinct from the controls (Fig. 3*G*). Thus, the presence of *PIK3CA* gain-of-function mutation in Schwann cells is associated with aerobic glycolysis-related characteristics.

Therapeutic Perspective for Patients with Severe *PIK3CA*-Related Nerve Disorders. Patient with PIK3CA mutation affecting the peripheral nerves frequently experience intense neurological pain, numbness, and motor limitation. We wondered whether alpelisib, a PIK3CA pharmacological inhibitor (29–33), could improve their conditions. Alpelisib has been recently granted accelerated approval by the US Food and Drug Administration (FDA) for patients with PROS but its impact on nerve anomalies related to PROS is unknown. In order to address this question, we started by treating *PIK3CA*$^{MPZ\text{-}Cre+}$ mice with a preexisting severe phenotype (P60) with alpelisib. Despite administering alpelisib daily, there were no significant changes observed in mouse survival or improvement in neurological symptoms (Fig. 4*A*). MRI performed at the age of P90 (4 wk on treatment) showed that alpelisib had a moderate impact on the neurolemma volume (Fig. 4*B*) but significantly improved the skin thickness (*SI Appendix*, Fig. S6*A*). Semithin section analysis of sciatic nerves at P90 showed that the area as the myelinated fibers were similar between mutant vehicle-treated and alpelisib-treated nerves whereas the number of aberrant fibers was modestly decreased in mutant alpelisib-treated nerves (Fig. 4*C*). Western blot and immunofluorescence studies of sciatic nerves revealed that AKT phosphorylation was not affected by alpelisib (Fig. 4 *D* and *E* and *SI Appendix*, Fig. S6*B*). Based on these findings, we administered alpelisib at an earlier time point, starting from P21. The earlier administration of alpelisib resulted in a delay in the onset of neurological symptoms and a notable extension in the overall survival of the mice (Fig. 4*A* and *SI Appendix*, Fig. S6*C*). Nevertheless, the mice still developed neurological abnormalities as they aged. MRI performed at P90 (9 wk on treatment) of age showed moderate neurolemma hypertrophy (Fig. 4*B*) with correction of the skin thickness (*SI Appendix*, Fig. S6*A*). Mice were then killed and semithin section analysis revealed the persistence of morphological alterations in the nerve (Fig. 4*C*). Consistently, Western blot and immunofluorescence studies of sciatic nerves revealed that AKT phosphorylation was partially blunted by alpelisib (Fig. 4 *D* and *E* and *SI Appendix*, Fig. S6*B*). On the basis of these results, we decided to initiate alpelisib early after birth, starting at P10. Very early administration of alpelisib led to an improvement in neurological symptoms at P90. Furthermore, there was a significant reduction in the area of the nerve, in the number of aberrantly myelinated fibers and of degenerated fibers compared to mice treated with the vehicle control (*SI Appendix*, Fig. S7 *A–D*). Western blot and immunofluorescence analysis of the sciatic nerves revealed a significant decrease of AKT activation (*SI Appendix*, Fig. S7 *E* and *F*). In order to elucidate the differences in treatment efficacy between early and late administration, we formulated the hypothesis that the increased thickness of the nerve in aged mice could potentially impede the penetration of the drug. To investigate and validate this hypothesis, we isolated sciatic nerves from *PIK3CA*$^{MPZ\text{-}Cre+}$ mice at three distinct ages (P10, P21, and P60). Subsequently, we exposed them ex vivo to either alpelisib or vehicle for a duration of 8 h. We observed that alpelisib effectively inhibited AKT phosphorylation at both P10 and P21, but its inhibitory effect was no longer observed at P60 (Fig. 4*F*). Alternatively, the penetration of the drug across the nerve blood barrier is permissive at P10 but is not or strongly reduced at later time point. To further explore these hypotheses, we measured alpelisib concentration in the sciatic nerves of mice with early and late treatment. We observed that while alpelisib concentrations in the nerves of young mutant and control mice were similar, the concentration was significantly lower in the nerves of older *PIK3CA*$^{MPZ\text{-}Cre+}$ mice compared to age-matched controls (Fig. 4*G*).

Last, we investigated the impact of alpelisib on various plasma metabolites and noted that the treatment led to a restoration of the majority of them. This effect was more pronounced when alpelisib was initiated early compared to late introduction (*SI Appendix*, Fig. S8 *A* and *B*).

Discussion

In this study, we present the outcomes of *PIK3CA* gain-of-function mutations in Schwann cells. To investigate the effects, we developed a mouse model that exhibited a severe neurological phenotype and endocrine abnormalities similar to those observed in patients with *PIK3CA*-related neuropathies. Additionally, we provided evidence of a communication pathway between the mutant cells and the surrounding tissues, leading to excessive growth of adipocytes and hyperplasia of hair follicles. Our findings indicate that the early administration of alpelisib, compared to delayed administration, improved the mouse phenotype likely because the drug penetrates more easily in small nerves with thinner perineurial tissues and in younger animals the nerve blood barrier is likely more permissive. Alternatively, the progression of the phenotype is such to be hardly reverted or ameliorated when fiber degeneration and loss are already evident.

The AKT/mTOR pathway plays a crucial role in the process of myelination and has been extensively explored (14–21). Indeed, overactivation of AKT, either through activating mutations or when PTEN is conditionally removed from Schwann cells, leads to localized excessive myelination and abnormal myelin formation (16–21). The impact of mTORC1 overactivation on myelination varies depending on the degree and timing of the overactivation (16, 17)· (18). Elevated mTORC1 activity during the transition from the promyelinating to the myelinating stage inhibits Schwann cell proliferation and delays the onset of myelination (16, 17). Conversely, when mTORC1 activity is moderately to highly increased at a later stage of nerve development, it causes localized excessive myelination and abnormal myelin formation (19–21). The observed phenotype resulting from PIK3CA overactivation

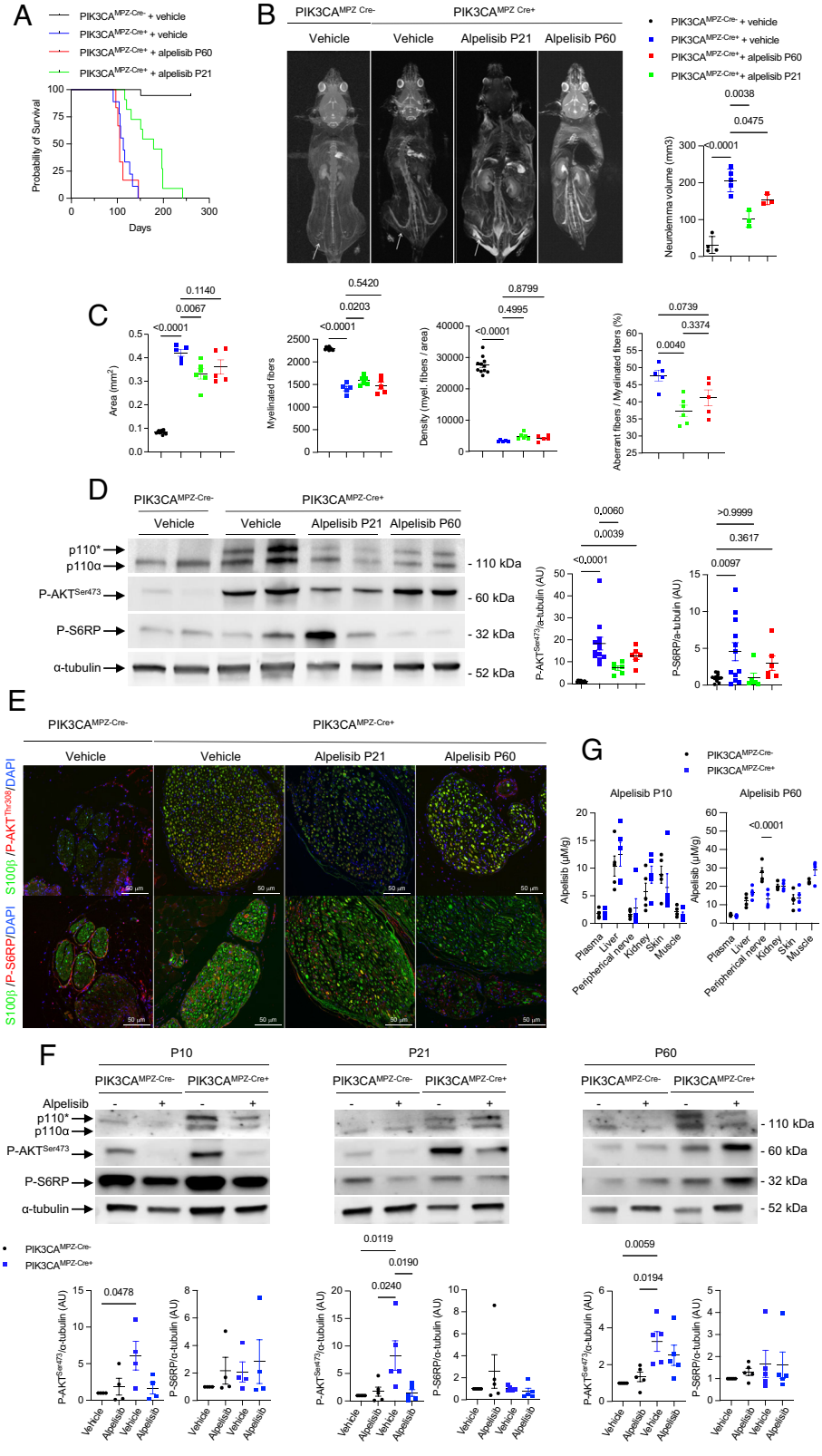

Fig. 4. Alpelisib improves *PIK3CA*$^{MPZ\text{-}Cre+}$mice outcome depending on their ages. (*A*) Kaplan–Meier survival curves of *PIK3CA*$^{MPZ\text{-}Cre-}$ and *PIK3CA*$^{MPZ\text{-}Cre+}$ mice treated with vehicle, alpelisib starting at either P21 or P60. (*B*) Whole-body T2-weighted MRI at P90 of *PIK3CA*$^{MPZ\text{-}Cre-}$, *PIK3CA*$^{MPZ\text{-}Cre+}$ vehicle-treated, *PIK3CA*$^{MPZ\text{-}Cre+}$-treated with either alpelisib started at P21 or P60. Neurolemma volume quantification. (*C*) Semithin section analysis of sciatic nerves at P90 of *PIK3CA*$^{MPZ\text{-}Cre-}$ and *PIK3CA*$^{MPZ\text{-}Cre+}$ mice treated with vehicle, alpelisib starting at either P21 or P60. The graphs show the quantification of area, myelinated fibers, density (myelinated fibers on area), and percentage of aberrant fibers on myelinated fibers. (*D*) Western blot and quantification of p110, AKT phosphorylation on residues Ser^{473} and S6RP in sciatic nerves of *PIK3CA*$^{MPZ\text{-}Cre-}$, *PIK3CA*$^{MPZ\text{-}Cre+}$ vehicle-treated, *PIK3CA*$^{MPZ\text{-}Cre+}$-treated mice with either alpelisib started at P21 or P60. (*E*) Representative immunofluorescence costaining of S100β and P-AKT^{Thr308} in sciatic nerves of *PIK3CA*$^{MPZ\text{-}Cre-}$, *PIK3CA*$^{MPZ\text{-}Cre+}$ vehicle-treated, *PIK3CA*$^{MPZ\text{-}Cre+}$-treated mice with either alpelisib started at P21 or P60 (*Upper*). Representative immunofluorescence costaining of S100β and P-S6RP in sciatic nerves of *PIK3CA*$^{MPZ\text{-}Cre-}$, *PIK3CA*$^{MPZ\text{-}Cre+}$ vehicle-treated, *PIK3CA*$^{MPZ\text{-}Cre+}$-treated mice with either alpelisib started at P21 or P60 (*Lower*). (*F*) Western blot and quantification of p110, AKT phosphorylation at Ser^{473} and S6RP in isolated sciatic nerves of *PIK3CA*$^{MPZ\text{-}Cre-}$ or *PIK3CA*$^{MPZ\text{-}Cre+}$ mice that were then treated ex vivo with either vehicle or alpelisib for 8 h. Sciatic nerves were collected at P7, P21, and P60. (*G*) Alpelisib measurements in plasma and tissues of *PIK3CA*$^{MPZ\text{-}Cre-}$ or *PIK3CA*$^{MPZ\text{-}Cre+}$ mice treated with alpelisib started either at P10 or P60.

was characterized by a delayed onset of myelination, which was then followed by the development of abnormal myelination accompanied by rapid deterioration and loss of fibers. Other downstream targets that could be recruited may provide an explanation for the phenotypic differentiation between PI3KCA and AKT/mTOR activation. It is important to note that the p110* mutant used in this study has been shown to more robustly recruit the AKT/mTOR pathway compared to the common PIK3CA variant observed in humans and may contribute to the severity of the phenotype observed in the mouse model (4).

The important finding in this study is the increasing body of evidence that highlights a communication between mutated cells and the neighboring healthy cells. We observed a significant correlation between *PIK3CA* mutation in Schwann cells and both adipose tissue and hair growth in both mouse models and human patients. It is worth noting that, in patient with *PIK3CA* mutation, the presence

of lipomatosis around neural anomalies is frequently observed (3, 5–9). Here, we show that, in these cases, patients carry the mutation exclusively in Schwann cells and not in adipocytes. Indeed, this works highlights the tight connection between Schwann cells, adipose tissue, and hair follicles. It has long been suggested that PIK3CA mutations may be associated with a non-cell autonomous effect; this had never been proven before. In biopsies taken from overgrowth sites in patients, the low PIK3CA variant allele frequency, combined with diffuse AKT phosphorylation and the presence of multiple cell types from different embryonic lineages, led to this hypothesis (34). This phenomenon has been observed across various tissue types (35). Here, we provide evidence that PIK3CA-mutated cells may exert a non-cell autonomous effect. This finding opens broad avenues of investigation to identify putative secreted factors that could be crucial for understanding disease development, as well as potential new biomarkers or therapeutic targets. Furthermore, given the high frequency of PIK3CA mutations in oncology, this finding may have significant implications for cancer research.

Finally, we found that alpelisib exhibited the ability to enhance the conditions of mice with *PIK3CA*-related disorders. Additionally, it demonstrated an early penetration into the myelin sheath as opposed to when introduced at later stages.

In conclusion, we report the outcomes resulting from a gain-of-function mutation in *PIK3CA* using a preclinical model. We have identified potential interactions between mutant and healthy cells and ultimately demonstrate that alpelisib can ameliorate the disease; however, its efficacy may be constrained within a specific time period.

Data, Materials, and Software Availability. All data needed to evaluate the conclusions in the paper are present in the paper and/or the *SI Appendix*.

ACKNOWLEDGMENTS. This study was supported by the European Research Council (CoG 2020 grant number 101000948 awarded to G.C.), the Agence Nationale de la Recherche–Programme d'Investissements d'Avenir (ANR-18-RHUS-005 to G.C.) and the Agence Nationale de la Recherche–Programme de Recherche Collaborative (19-CE14-0030-01 to G.C.). This work was also supported by the CLOVES SYNDROME COMMUNITY (West Kennebunk, USA), Association Syndrome de CLOVES (Nantes, France), Fondation d'entreprise IRCEM (Roubaix, France), Fonds de dotation Emmanuel BOUSSARD (Paris, France), the Fondation DAY SOLVAY (Paris, France), the Fondation TOURRE (Paris, France) to G.C., the Fondation BETTENCOURT SCHUELLER (Paris, France) to GC, the Fondation Line RENAUD-Loulou GASTE (Paris, France), the Fondation Schlumberger pour l'Education et la Recherche (Paris, France), the Association Robert Debré pour la Recherche Médicale awarded to G.C., a grant (Signalopathies) from MSD Avenir to G.C., WonderFIL smiles–a Facial Infiltrating Lipomatosis community (Norway), INSERM, Assistance Publique Hôpitaux de Paris, l'Université Paris Cité and Fondation pour la Recherche Médicale (FDM202006011222) awarded to G.M. We are also very grateful to our generous donors. Research in the Bolino laboratory is currently supported by the Muscular Dystrophy Association (#MDA 957250), Fondazione Telethon (#GGP20063), the Charcot–Marie–Tooth Association USA, and the Charcot–Marie–Tooth Research Foundation USA. In vivo preclinical imaging was performed at the Life Imaging Facility of the University of Paris (Plateforme Imageries du Vivant), supported by France Life Imaging (grant ANR-11-INBS-0006) and Infrastructures BiologieSanté.

Author affiliations: [a]Université Paris Cité, Paris 75015, France; [b]INSERM U1151, Institut Necker-Enfants Malades, Paris 75015, France; [c]Unité de Médecine Translationnelle et Thérapies Ciblées, Hôpital Necker-Enfants Malades, Assistance Publique Hôpitaux de Paris, Paris 75015, France; [d]Division of Neuroscience, Human Inherited Neuropathies Unit, Institute of Experimental Neurology, Ospedale San Raffaele, Milan 20132, Italy; [e]Service d'Imagerie Pédiatrique, Hôpital Femme-Mère-Enfant, Hospices Civiles de Lyon, Bron 69500, France; [f]Centre de Recherche en Acquisition et Traitement de l'Image pour la Santé UMR 5220, Villeurbanne 69100, France; [g]Service de Radiologie Mère-Enfant, Hôpital Nord, Saint Etienne 42270, France; [h]Sorbonne Université, Inserm, Centre de Recherche en Myologie, Paris 75013, France; [i]Laboratoire d'Anatomie Pathologique, Hôpital Necker-Enfants Malades, Assistance Publique Hôpitaux de Paris, Paris 75015, France; [j]Laboratoire d'Oncohématologie, Hôpital Necker-Enfants Malades, Assistance Publique Hôpitaux de Paris, Paris 75015, France; [k]Plateforme Imageries du Vivant, Université de Paris, Paris Centre de Recherche Cardiovasculaire, INSERM, Paris 75015, France; [l]Necker Bio-Image Analysis, INSERM US24/CNRS UMS 3633, Paris 75015, France; and [m]Vita-Salute San Raffaele University, Milan 20132, Italy

Author contributions: A.B. and G.C. designed research; Q.V., M.F., S.L., C.B., S.M., R.D.G., A.F., C.H., S.P., G.M., F.M., S.F., E.B., S.K., P.V., V.A., T.V., G.A., and B.T. performed research; Q.V., M.F., S.L., C.B., S.M., R.D.G., C.H., S.P., and G.G. contributed new reagents/analytic tools; Q.V., M.F., S.L., C.B., S.M., R.D.G., A.F., C.H., S.P., S.F., E.B., S.K., P.V., V.A., T.V., G.A., N.G., L.G., A.B., and G.C. analyzed data; and Q.V., A.B., and G.C. wrote the paper.

Competing interest statement: G.C. receives or has received consulting fees from Novartis, Fresenius Medical Care, Vaderis, Alkermes, IPSEN and BridgeBio. The other authors declare no other competing interests. A patent application ("BYL719 (alpelisib) for use in the treatment of PIK3CArelated overgrowth spectrum" #WO2017140828A1) has been filed by INSERM, CNRS, Université Paris Cité, and Assistance Publique-Hôpitaux De Paris (AP-HP) for the use of BYL719 (alpelisib) in the treatment of PIK3CA-related overgrowth spectrum (PROS/CLOVES syndrome). G.C. is the inventor. This patent is licensed to Novartis. A patent application ("Methods for monitoring and treating Warburg effect in patients with PI3K-related disorders" #EP22305091) has been filed by INSERM, CNRS, Université Paris Cité, and AP-HP for the monitoring and treatment of Warburg effect in patients with PI3K-related disorders. S.L. and G.C. are the inventors.

1. B. Bilanges, Y. Posor, B. Vanhaesebroeck, PI3K isoforms in cell signalling and vesicle trafficking. *Nat. Rev. Mol. Cell Biol.* **20**, 515–534 (2019), 10.1038/s41580-019-0129-z.
2. H. C. Welch, W. J. Coadwell, L. R. Stephens, P. T. Hawkins, Phosphoinositide 3-kinase-dependent activation of Rac. *FEBS Lett.* **546**, 93–97 (2003).
3. G. Canaud, A. M. Hammill, D. Adams, M. Vikkula, K. M. Keppler-Noreuil, A review of mechanisms of disease across PIK3CA-related disorders with vascular manifestations. *Orphanet. J. Rare Dis.* **16**, 306 (2021).
4. Q. Venot *et al.*, Targeted therapy in patients with PIK3CA-related overgrowth syndrome. *Nature* **558**, 540–546 (2018).
5. P. R. Blackburn *et al.*, PIK3CA mutations in lipomatosis of nerve with or without nerve territory overgrowth. *Mod. Pathol.* **33**, 420–430 (2020).
6. T. Marek *et al.*, Expanding the phenotypic spectrum of lipomatosis of the sciatic nerve: Early-onset colonic diverticular disease. *Neurogastroenterol. Motil.* **32**, e13917 (2020).
7. B. A. Ebner *et al.*, Brachial plexus lipomatosis with perineurial pseudoonion bulb formation: Result of a mosaic *PIK3CA* mutation in the para-axial mesoderm state *Brain Pathol.* **32**, e13057 (2022).
8. X. F. Shen, K. Gasteratos, G. A. Spyropoulou, F. Yin, Y. J. Rui, Congenital difference of the hand and foot: Pediatric macrodactyly. *J. Plast. Reconstr. Aesthet. Surg.* **75**, 4054–4062 (2022).
9. J. Osterloh *et al.*, PIK3CA mutation testing as a valuable molecular surrogate for lipomatosis of the median nerve: Clinicopathological and molecular analysis of six cases. *Virchows Arch.* **483**, 33–39 (2023), 10.1007/s00428-023-03540-7.
10. T. Marek, K. K. Amrami, R. J. Spinner, Occult lipomatosis of the nerve as part of macrodystrophia lipomatosa: Illustrative case. *J. Neurosurg. Case Lessons* **5**, 2463 (2023).
11. I. G. Koutlas, *et al.*, Orofacial overgrowth with peripheral nerve enlargement and perineuriomatous pseudo-onion bulb proliferations is part of the. *HGG Adv.* **1**, 100009 (2020).
12. A. A. Maldonado, R. J. Spinner, J. M. Carter, C. J. Klein, Letter to editor: Orofacial overgrowth with peripheral nerve enlargement and perineuriomatous pseudo-onion bulb proliferations is part of the PIK3CA-related overgrowth spectrum. *Hum. Genet. Genomics Adv.* **3**, 100110 (2022).
13. W. Chen, X. Tian, L. Chen, W. Huang, Macrodactyly of the foot resulting from plantar nerve impairment. *J. Plast. Reconstr. Aesthet. Surg.* **74**, 1840–1847 (2021).
14. T. Marek *et al.*, What's known and what's new in adipose lesions of peripheral nerves? *Acta Neurochir.* **163**, 835–842 (2021).
15. J. L. Salzer, Schwann cell myelination. *Cold Spring Harb. Perspect. Biol.* **7**, a020529 (2015).
16. E. Domenech-Estevez *et al.*, Akt regulates axon wrapping and myelin sheath thickness in the PNS. *J. Neurosci.* **36**, 4506–4521 (2016).
17. S. Goebbels *et al.*, Genetic disruption of Pten in a novel mouse model of tomaculous neuropathy. *EMBO Mol. Med.* **4**, 486–499 (2012).
18. X. X. Li *et al.*, Schwann cell-specific Pten inactivation reveals essential role of the sympathetic nervous system activity in adipose tissue development. *Biochem. Biophys. Res. Commun.* **531**, 118–124 (2020).
19. B. Beirowski, K. M. Wong, E. Babetto, J. Milbrandt, mTORC1 promotes proliferation of immature Schwann cells and myelin growth of differentiated Schwann cells. *Proc. Natl. Acad. Sci. U.S.A.* **114**, E4261–E4270 (2017).
20. G. Figlia, C. Norrmen, J. A. Pereira, D. Gerber, U. Suter, Dual function of the PI3K-Akt-mTORC1 axis in myelination of the peripheral nervous system *Elife* **6**, e29241 (2017).
21. G. Figlia, D. Gerber, U. Suter, Myelination and mTOR. *Glia* **66**, 693–707 (2018).
22. D. L. Sherman *et al.*, Arrest of myelination and reduced axon growth when Schwann cells lack mTOR. *J. Neurosci.* **32**, 1817–1825 (2012).
23. C. Norrmen *et al.*, *M*TORC1 controls PNS myelination along the *M*TORC1-RXRgamma-SREBP-lipid biosynthesis axis in Schwann cells. *Cell Rep.* **9**, 646–660 (2014).
24. M. L. Feltri *et al.*, A novel P0 glycoprotein transgene activates expression of lacZ in myelin-forming Schwann cells. *Eur. J. Neurosci.* **11**, 1577–1586 (1999).
25. S. Muller-Rover *et al.*, A comprehensive guide for the accurate classification of murine hair follicles in distinct hair cycle stages. *J. Investig. Dermatol.* **117**, 3–15 (2001).
26. H. B. Chase, W. Montagna, J. D. Malone, Changes in the skin in relation to the hair growth cycle. *Anat. Rec.* **116**, 75–81 (1953).
27. S. Ladraa *et al.*, PIK3CA gain-of-function mutation in adipose tissue induces metabolic reprogramming with Warburg-like effect and severe endocrine disruption. *Sci. Adv.* **8**, eade7823 (2022).

28. P. Magnani *et al.*, Glucose transporters in rat peripheral nerve: Paranodal expression of GLUT1 and GLUT3. *Metab. Clin. Experim.* **45**, 1466–1473 (1996).
29. G. Canaud *et al.*, Alpelisib for treatment of patients with PIK3CA-related overgrowth spectrum (PROS) *Genet. Med.* **25**, 100969 (2023), 10.1016/j.gim.2023.100969.
30. L. Zerbib *et al.*, Targeted therapy for capillary-venous malformations. *Signal Transduct. Target. Ther.* **9**, 146 (2024).
31. F. Delestre *et al.*, Alpelisib administration reduced lymphatic malformations in a mouse model and in patients. *Sci. Transl. Med.* **13**, eabg0809 (2021).
32. C. Bayard *et al.*, Hemifacial myohyperplasia is due to somatic muscular *PIK3CA* gain-of-function mutations and responds to pharmacological inhibition *J. Exp. Med.* **220**, e20230926 (2023).
33. G. Morin *et al.*, Treatment of two infants with PIK3CA-related overgrowth spectrum by alpelisib. *J. Exp. Med.* **219**, e20212148 (2022).
34. R. R. Madsen, B. Vanhaesebroeck, R. K. Semple, Cancer-associated PIK3CA mutations in overgrowth disorders. *Trends Mol. Med.* **24**, 856–870 (2018).
35. A. Fraissenon *et al.*, Sotorasib for vascular malformations associated with KRAS G12C mutation. *N. Engl. J. Med.* **391**, 334–342 (2024).